

ARF60 AUS-UAV MODELING, SYSTEM IDENTIFICATION, GUIDANCE AND CONTROL: VALIDATION THROUGH HARDWARE IN THE LOOP SIMULATION

Amer Al-Radaideh, M.A.Al-Jarrah, Ali Jhemi, and R.Dhaouadi

American University of Sharjah
Mechatronics Graduate Program
P.O.Box 26666, Sharjah, U.A.E
b00025637@aus.edu

ABSTRACT

Automatic control of Unmanned Aerial Vehicles (UAVs) has been a growing area of research in aerospace technology for a long time, yet this area needs a great deal of development in order to get a reliable autonomous system capable of performing all types of maneuvers with high degree of stability and desired performance. In this paper, the development and building of a fully functioning test bed UAV platform is illustrated. The test-bed includes an enhanced hardware in the loop simulation "HILS" system to facilitate the development of the flight control system (FCS). Furthermore, the design of the guidance laws, autopilots implementation on the embedded system were integrated with the Hardware in the Loop Simulation (HILS). Finally, trajectory following results were demonstrated.

1. INTRODUCTION

Unmanned Aerial Vehicles (UAV's) have gained increasing considerations due to their low cost and improved autonomy. UAV's have been employed in numerous applications, civilian as well as military. Applications include surveillance, object tracking, and crop dusting. UAVs are increasingly becoming more independent with an ever increasing intelligence and decision making capabilities. These capabilities are being programmed into the embedded systems thanks to the availability of low cost microcontrollers, sensors, and actuators systems.

Current UAV research considers low level flight control algorithms, or auto-piloting, to improve the following subjects: Guidance, trajectory tracking, path planning coupled with intelligent adaptive mission capability, multi-UAV coordination, and aerial aerobatics and stern flight maneuvers. These areas of research have been stimulated with recent commercial off-the-shelf (COTS) hardware, affordable avionics, and reliable navigation systems.

This paper focuses on the design and building of a fully functional UAV test bed platform. The test-bed will include an enhanced hardware in the loop simulation "HILS" system designed to facilitate the development of the flight control system (FCS) and the guidance and navigation system.

However, this paper emphasized the guidance/control laws design and implementations on the embedded system, as well as the testing and validation on the Hardware in the Loop Simulation (HILS).

The paper is organized as follow: Section 2 explains the dynamical model and the nonlinear mathematical equations. The ARF60 AUS-UAV modeling and system identifications are addressed in Section 3. The controller design and simulation of the

ARF60 AUS-UAV are presented in Section 4. Section 5 covers the hardware in the loop simulation (HILS) as well as the real-time trajectory tracking are presented. Finally, conclusions are addressed in Section 6.

2. ARF60 AUS-UAV NONLINEAR MODEL AND DYNAMICS EQUATIONS

The standard 6-DOF equations of motion for a conventional aircraft are used for the modeling and simulation of a small size UAV. The Earth can be assumed to be flat when the vehicle is operating over a small area. The body-axes force, moments, kinematics and navigations equations are described below:

- Force equations:

$$\begin{pmatrix} \dot{u} \\ \dot{v} \\ \dot{w} \end{pmatrix} = \begin{pmatrix} rv - qw \\ pw - ru \\ qu - pv \end{pmatrix} + 1/m \begin{pmatrix} f_x \\ f_y \\ f_z \end{pmatrix} \quad (1a)$$

$$\begin{pmatrix} \dot{x} \\ \dot{y} \\ \dot{z} \end{pmatrix} = \begin{pmatrix} f_{gx} \\ f_{gy} \\ f_{gz} \end{pmatrix} + \begin{pmatrix} f_{ax} \\ f_{ay} \\ f_{az} \end{pmatrix} + \begin{pmatrix} f_{Tx} \\ f_{Ty} \\ f_{Tz} \end{pmatrix} \quad (1b)$$

$$\begin{pmatrix} f_{gx} \\ f_{gy} \\ f_{gz} \end{pmatrix} = \begin{pmatrix} -mg \sin \theta \\ mg \cos \theta \sin \phi \\ mg \cos \theta \cos \phi \end{pmatrix} \quad (1c)$$

$$\begin{pmatrix} f_{ax} \\ f_{ay} \\ f_{az} \end{pmatrix} = \begin{pmatrix} \frac{1}{2} \rho V_{air}^2 SCx \\ \frac{1}{2} \rho V_{air}^2 SCy \\ \frac{1}{2} \rho V_{air}^2 SCz \end{pmatrix} \quad (1d)$$

where:

f_g : gravitational forces.

f_a : aerodynamic forces.

f_T : forces due to thrust.

ϕ : Roll angle.

θ : Pitch angle.

ψ : Yaw angle.

S : wing area total.

V_{air} : The true UAV airspeed.

u : X-axis velocity in the body frame.

v : Y-axis velocity in the body frame.

w : Z-axis velocity in the body frame.

p : Roll rate.

q : Pitch rate.

r : Yaw rate.
 C_X : Drag force aerodynamic coefficient.
 C_Y : Side force aerodynamic coefficient.
 C_Z : Lift force aerodynamic coefficient.
 m : Aircraft mass.
 ρ : Air density.

• Moment Equations:

$$\begin{pmatrix} \dot{p} \\ \dot{q} \\ \dot{r} \end{pmatrix} = \begin{pmatrix} \Gamma_1 pq - \Gamma_2 qr \\ \Gamma_5 pr - \Gamma_4(p^2 - r^2) \\ \Gamma_6 pq - \Gamma_1 qr \end{pmatrix} + \begin{pmatrix} \Gamma_3 L + \Gamma_4 N \\ \frac{1}{J_y} M \\ \Gamma_4 L + \Gamma_7 N \end{pmatrix} \quad (2a)$$

where:

$$\Gamma \triangleq J_x J_z - J_{xz}^2 \quad (2b)$$

$$\Gamma_1 = \frac{J_{xz}(J_x - J_y + J_z)}{\Gamma} \quad (2c)$$

$$\Gamma_2 = \frac{J_z(J_z - J_y) + J_{xz}^2}{\Gamma} \quad (2d)$$

$$\Gamma_3 = \frac{J_z}{\Gamma} \quad (2e)$$

$$\Gamma_4 = \frac{J_{xz}}{\Gamma} \quad (2f)$$

$$\Gamma_5 = \frac{J_z - J_x}{J_y} \quad (2g)$$

$$\Gamma_6 = \frac{1}{J_y} \quad (2h)$$

$$\Gamma_7 = \frac{J_x(J_x - J_y) + J_{xz}^2}{\Gamma} \quad (2i)$$

$$\Gamma_8 = \frac{J_x}{\Gamma} \quad (2j)$$

where:

J_x : Moment of inertia in the body x-axis.
 J_y : Moment of inertia in the body y-axis.
 J_z : Moment of inertia in the body z-axis.
 J_{xz} : Product of inertia of x & z axes.

$$\begin{pmatrix} L \\ M \\ N \end{pmatrix} = \begin{pmatrix} \frac{1}{2} \rho V_{air}^2 S b C_l \\ \frac{1}{2} \rho V_{air}^2 S \bar{c} C_m \\ \frac{1}{2} \rho V_{air}^2 S b C_n \end{pmatrix} \quad (2k)$$

where:

C_ℓ : X-axis aerodynamic moment coefficient.
 C_m : Y-axis aerodynamic moment coefficient.
 C_n : Z-axis aerodynamic moment coefficient.

• Navigation equations:

$$\begin{pmatrix} \dot{x} \\ \dot{y} \\ \dot{h} \end{pmatrix} = \begin{pmatrix} c\theta c\psi & s\phi s\theta c\psi - s\psi c\phi & c\phi s\theta c\psi + s\psi s\phi \\ c\theta s\psi & c\phi s\theta s\psi + s\psi c\phi & c\phi s\theta s\psi - c\psi s\phi \\ -s\theta & s\phi c\theta & c\phi c\theta \end{pmatrix} \begin{pmatrix} u \\ v \\ w \end{pmatrix} \quad (3)$$

$$\begin{pmatrix} \dot{\phi} \\ \dot{\theta} \\ \dot{\psi} \end{pmatrix} = \begin{pmatrix} 1 & \sin \phi \tan \theta & \cos \phi \tan \theta \\ 0 & \cos \phi & -\sin \phi \\ 0 & \sin \phi \sec \theta & \csc \phi \sec \theta \end{pmatrix} \begin{pmatrix} p \\ q \\ r \end{pmatrix} \quad (4)$$

3. ARF60 AUS-UAV MODELING AND SYSTEM IDENTIFICATIONS

3.1. ARF60 AUS-UAV Simulink Nonlinear Model

The equations of motion, including forces and moments are modelled in the Simulink environment. Simulink Modeling is simple, more flexible, and user-friendly compared to other software packages, see reference [2]. With the convenience of Simulink Aerosim and Aerospace Blocksets, building, modifying and maintaining a model is straightforward task. Figure 1 shows the general structure of the ARF60 AUS-UAV Simulink nonlinear model.

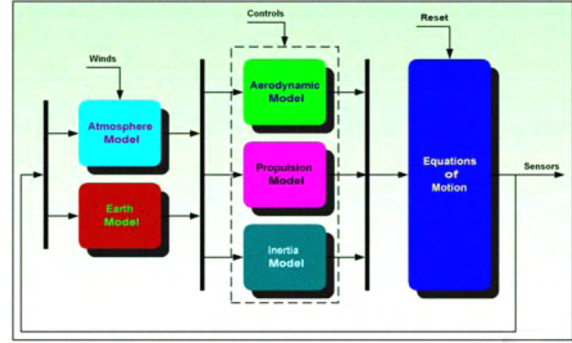


Figure 1: ARF60 UAV Simulink Model general Structure.

Most of the model subsystems were built using the Aerosim and Aerospace tool boxes. The propulsion and actuator models were derived experimentally as described in Sections 3.4 and 3.5. The aerodynamics, propulsion, and inertia subsystems compute the airframe loads (forces and moments) as functions of control inputs and flight states. The resulting accelerations are integrated once to obtain the aircraft velocities, then integrated second to obtain aircraft positions. The computed aircraft states are subsequently used to compute forces and moments needed for next iteration.

3.2. Aerodynamic Numerical Modeling

Aircraft aerodynamics can be modelled using linear estimated coefficients based on aircraft geometry. Aircraft CG location and mass properties are very important parameters need to be identified. The center of gravity location was carefully determined in the body axes; it was taken at the point where the aircraft has a static balance. Two lines were drawn on the two planes ($x-y$ & $x-z$). Another line was drawn on the ($x-y$) to get the intersection with the depth of the ($x-z$) mark; Figure 2. The gross and empty weight of the UAV and the landing wheels were measured using accurate scale. Payload items, (ie.IMU, Autopilot, batteries, etc.), were weighed afterwards. To estimate the stability derivatives, all needed data listed in Table 1 was included in a MATLAB script. The computed stability derivatives are summarized in Table 2.

Table 1: ARF60 measured geometric parameters - input to the MATLAB script

Property	Symbol	Value	Unit(SI)
Empty A/C Mass	m_E	3.416	Kg
Gross A/C Mass	m_G	3.5105	Kg
CG Location (x)	CG	-0.0130	m
CG Location (y)	CG	0.00	m
CG Location (z)	CG	-0.0800	m
Roll Inertia	J_x	0.19969	$kg.m^2$
Pitch Inertia	J_y	0.24086	$kg.m^2$
Yaw Inertia	J_z	0.396	$kg.m^2$
Wing			
Length of MAC	\bar{C}	0.324	m
Wing Span	b	1.87	m
Wing Dihedral Angle	Γ	6	deg
Wing Taper Ratio	λ	1	—
Wing Surface Area	S	0.6059	m^2
Ailerons Surface Area	S_a	0.0581	m^2
Ailerons Around Area	A_a	0.4277	m^2
Horizontal Tail			
Horizontal Tail Span	b_t	0.6700	m
Horizontal Tail MAC	\bar{C}_t	0.1950	m
Horizontal Tail Area	S_t	0.1307	m^2
Elevator Surface Area	S_e	0.0232	m^2
Dist. from CG to H.Tail Q-Cord	l_t	0.8200	m
Horizontal Tail Volume Ratio	V_H	0.5457	—
Vertical Tail			
Vertical Tail Span	b_v	0.2350	m
Vertical Tail MAC	\bar{C}_v	0.2150	m
Vertical Tail Area	S_v	0.0505	m^2
Rudder Surface Area	S_r	0.1307	m^2
Dist. from CG to V.Tail AC	l_t	0.8400	m
Vertical Tail Volume Ratio	V_v	0.2162	—

Table 2: Stability derivatives of the ARF60 UAV (All units per radian)

Symbol	Derivative	Value
Lift coefficient		
C_{L_0}	Zero alpha lift	0.4100
C_{L_α}	Alpha derivative	4.3842
$C_{L_{\alpha_t}}$	Alpha derivative for the tail	3.6369
$C_{L_{\alpha_v}}$	Alpha derivative for the vertical tail	0.9114
$C_{L_{\delta_e}}$	Pitch control (elevator) derivative	0.3059
$C_{L_{\dot{\alpha}}}$	Alpha-dot derivative	0
C_{L_q}	Pitch rate derivative	0.6431
Drag coefficient		
C_{D_0}	Minimum drag	0.0500
$C_{D_{\delta_e}}$	Pitch control (elevator) derivative	0
$C_{D_{\delta_a}}$	Roll control (aileron) derivative	0
$C_{D_{\delta_r}}$	Yaw control (rudder) derivative	0
Side force coefficient		
C_{Y_β}	Sideslip derivative	-0.1795
$C_{Y_{\delta_a}}$	Roll control derivative	0
$C_{Y_{\delta_r}}$	Yaw control derivative	0.1132
C_{Y_p}	Roll rate derivative	0
C_{Y_r}	Yaw rate derivative	0
Pitch moment coefficient		
C_{m_0}	Zero alpha pitch	0
C_{m_α}	Alpha derivative	0
$C_{m_{\delta_e}}$	Pitch control derivative	-0.7741
$C_{m_{\dot{\alpha}}}$	Alpha dot derivative	-6.0730
C_{m_q}	Pitch rate derivative	-10.0467
Roll moment coefficient		
C_{l_β}	Sideslip derivative	-0.0013
$C_{l_{\delta_a}}$	Roll control derivative	0.8275
$C_{l_{\delta_r}}$	Yaw control derivative	0.0036
C_{l_p}	Roll rate derivative	-1.8267
C_{l_r}	Yaw rate derivative	0.0052
Yaw moment coefficient		
C_{n_β}	Sideslip derivative	0.4653
$C_{n_{\delta_a}}$	Roll control derivative	-0.1357
$C_{n_{\delta_r}}$	Yaw control derivative	-0.2934
C_{n_p}	Roll rate derivative	-1.8267
C_{n_r}	Yaw rate derivative	-0.2934



Figure 2: CG location Experiment.

3.3. Aircraft Linear Model

The state space linear model of the aircraft was derived using the already available stability derivatives found in section 3.2. The linearized state space model is needed to develop the guidance and control laws. It is used to develop airspeed hold, altitude hold, and attitude hold as well as for ground and navigation control. The nonlinear aircraft model is linearized about several trim conditions. The longitudinal and lateral models were derived.

3.3.1. ARF60 UAV Longitudinal model

The following state space model is the linear longitudinal model for the ARF60 UAV linearized around a typical flight condition ($V_a = 20m/s$, $h = 100m$, and $\phi = 0$):

$$\begin{pmatrix} \dot{u} \\ \dot{w} \\ \dot{q} \\ \dot{\theta} \\ \dot{h} \end{pmatrix} = \begin{pmatrix} -0.2289 & 0.3712 & 0 & -9.81 & 0 \\ -1.8772 & -10.1512 & 20 & 0 & 0 \\ 0.9219 & -7.0403 & -26.072 & 0 & 0 \\ 0 & 0 & 1 & 0 & 0 \\ 0 & -1 & 0 & 20 & 0 \end{pmatrix} \begin{pmatrix} u \\ w \\ q \\ \theta \\ h \end{pmatrix} + \begin{pmatrix} 0 & 51.5 \\ -14.0042 & 0 \\ -147.6913 & 0 \\ 0 & 0 \\ 0 & 0 \end{pmatrix} \begin{pmatrix} \delta_e \\ \delta_t \end{pmatrix} \quad (5)$$

Where the state variables $(u \ w \ q \ \theta \ h)$ refer to the longitudinal velocities, u and w , the pitch rate, q and the angle of inclination, θ . In addition to the above states, the altitude h was added to account for the height above the ground. The control input $(\delta_e \ \delta_t)$ is the elevator deflection angle δ_e , and the engine throttle lever δ_t .

Table 3: Pole locations, natural frequencies and periods for the longitudinal modes.

	Eigenvalue (Pole)	$\omega_n(\text{rad/s})$	Period(s)
Mode 1 (phugoid mode)	$\lambda_{1,2} = -0.115 \pm 0.729i$	7.39e-001 (1.176 Hz)	8.5023
Mode 2 (short-period mode)	$\lambda_{3,4} = -18.111 \pm 8.807i$	2.01e+001 (3.2 Hz)	0.3126

Table 4: pole locations, natural frequencies and periods for the lateral modes.

	Eigenvalue (Pole)	$\omega_n(\text{rad/s})$	Period(s)
Mode 1 (Spiral/slow mode)	$\lambda_1 = 0.0027$	0.0027	2327.1
Mode 2 (Roll/fast mode)	$\lambda_2 = -47.3587$	47.3587	0.1327
Mode 3(Dutch Roll/ oscillatory mode)	$\lambda_3 = -6.5317 \pm 17.1635i$	18.3643	0.3421

The 4 poles yielded two complex conjugate pairs, one for short period (heavily damped) and one for phugoid (long) period (lightly damped). The eigenvalues of the system matrix A are listed in Table 3

3.3.2. ARF60 UAV Lateral model

Similar to the longitudinal model, the dynamics describing lateral perturbations about the same equilibrium trim conditions previously mentioned is written below in concise state space form. The eigenvalues of the system matrix A are listed in Table 4.

$$\begin{pmatrix} \dot{\beta} \\ \dot{p} \\ \dot{r} \\ \dot{\phi} \end{pmatrix} = \begin{pmatrix} -0.7684 & 0 & -1.0000 & 0.4905 \\ -1.7563 & -47.4848 & 0.3362 & 0 \\ 326.1682 & -17.9588 & -12.1661 & 0 \\ 0 & 1 & 0 & 0 \end{pmatrix} \begin{pmatrix} \beta \\ p \\ r \\ \phi \end{pmatrix} + \begin{pmatrix} 0 & 0.2591 \\ 1150.2319 & 5.0475 \\ -95.1241 & -205.6651 \\ 0 & 0 \end{pmatrix} \begin{pmatrix} \delta_a \\ \delta_r \end{pmatrix} \quad (6)$$

Where v is the sideslip velocity, p and r represent the roll and yaw rates and ϕ is the roll angle. The aileron control input is denoted by δ_a , and the rudder control input δ_r .

3.4. The Engine and Propeller System ID

To build a realistic aircraft model, the characterization of the engine response to throttle command need to be identified. Engine dynamics are function of the throttle and other several environment parameters such as: fuel inlet, manifold pressure, ambient temperature and air pressure. For simplicity, we assume that all inputs are constant and only the throttle is varied. An experiment has been conducted to get a transfer function that relates the throttle command to engine RPM and propeller thrust force output. The experiment was successfully carried on the engine-propeller set.

The data collected during this experiment consists of: engine thrust and the engine RPM. The thrust is measured using load cell

Table 5: OS 61FX Engine RPM System ID Results

Model	Model Structure	Fitting %
ARX	arx525	85.38%
ARMAX	amx5111	84.4 %
OE	oe2210	84.91%
BJ	bj11232	85.31%

Table 6: OS 61FX Engine Thrust System ID Results

Model	Model Structure	Fitting %
ARX	arx111	73.56%
ARMAX	amx1131	74.64%
OE	oe617	80.53%
BJ	bj51110	80.58%

while the RPM is measured using IR Reflective object sensor. The input signal is the duty cycle that controls the throttle and is represented by the pseudo random binary sequence to excite all dynamic modes of the system.

Using dSPACE, an experiment taking the throttle command as a pseudo random variable has been performed. The throttle command was fed to the throttle servo motor. The Engine RPM varied due to the change in fuel combustion rate. The encoder then read and sent the RPM data to dSPACE. Due to the rotation of the engine the propeller applied a thrust force on the aircraft. This force is measured by the load cell and its output is saved in dSPACE. Figure shows the block diagram for engine system identification experiment.

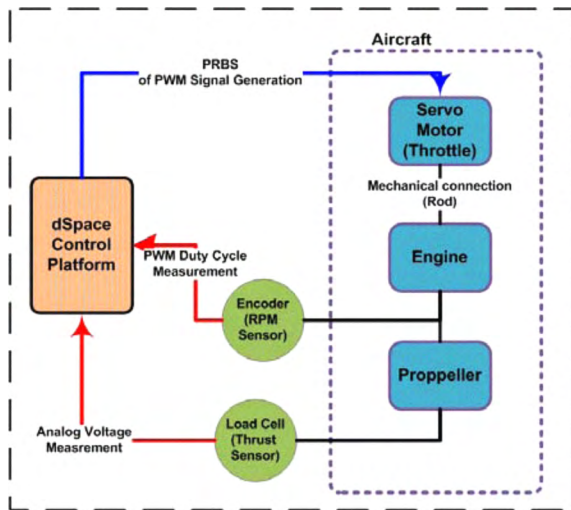


Figure 3: Engine Identification Experimental Block Diagram.

Identifying the OS 61FX Engine and its Propeller was conducted using various model structures including ARMAX, ARX, OE and BJ. The identification results from each model are summarized in Table 5.

From Table 5, the best model that describes the engine RPM dynamics is the BJ while the worst model is the ARMAX. Figure 4 shows graphical fitting percentage for each model structure.

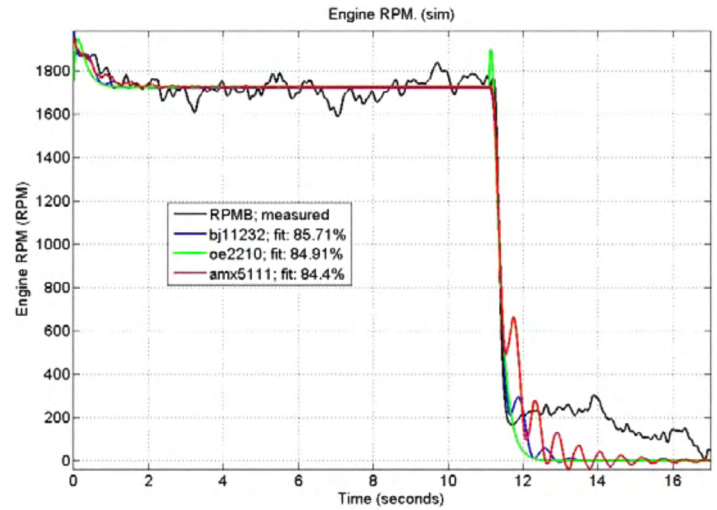


Figure 4: The RPM Measured Output with the Output from Various Identification Models

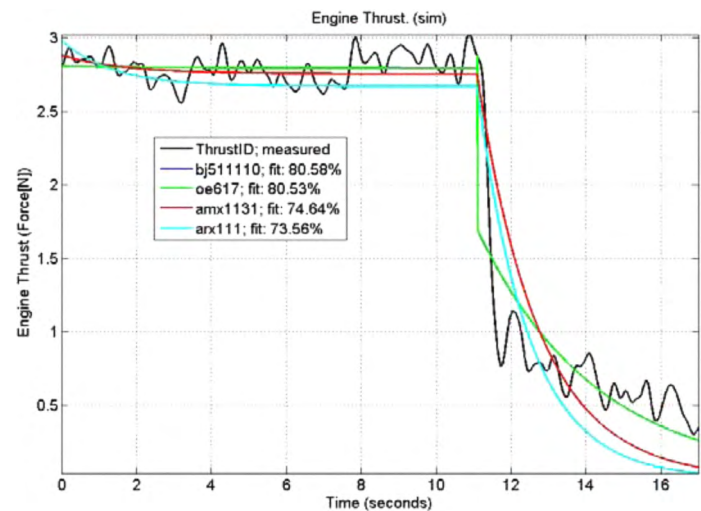


Figure 5: The Thrust Measured Output with the Output from Various Identification Models

On the other hand, Table 6, shows that the best model that describes the engine thrust dynamics is the BJ while the worst model is the ARX. Figure 5 shows graphical fitting percentage for each model structure.

3.5. Actuator System ID

Four identical R/C servo motors are used to actuate the UAV control surfaces. A mechanical link is used to couple each servo arm to the corresponding control surface. Figure 6 shows the experimental setup used for actuator identification. The collected data from the experiment were the servo position and the control commands. Deflection angles of the control surfaces were measured and calibrated using potentiometers linked to the servo motor and a digital encoder, respectively. Since an R/C servo motor nearly performs a dead beat control, a first-order low pass filter combined with control saturation produces a satisfactory actuator model. A common transfer function that describes the servo dynamics is presented in Equation 7.

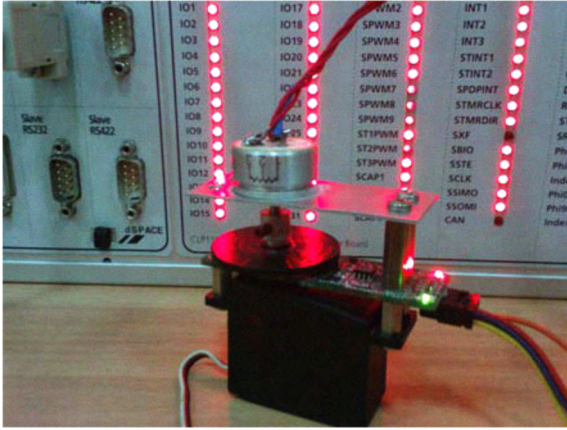


Figure 6: Actuator Identification Setup.

$$G(s) = \frac{1}{s + 8.757} \quad (7)$$

4. ARF60 AUS-UAV CONTROLLER DESIGN AND SIMULATION

4.1. ARF60 UAV Autopilot Design Using Successive Loop Closure (SLC)

The aircraft controller is composed of three subsystem controllers. These are: stability augmentation system (SAS) controller, the attitude stabilization (Autopilot) controller, and the trajectory tracking controller. The stability augmentation system provides artificial damping in order to suppress any high frequency aircraft dynamic. Furthermore, the attitude stabilizer regulates aircraft pitch and roll angles to control aircraft acceleration. Finally in the outer loop, the trajectory tracker controls heading and altitude. All the aforementioned controllers are divided into a longitudinal and lateral sets.

Successive loop closure technique had been used through the control law design. The basic idea is that only one loop is closed at

a time. At each stage of the design, there is only one gain to tune. Therefore, root locus techniques were used to design our control law using successive loop closure. Designing an autopilot using these techniques requires linear models of the UAV dynamics for a number of trimmed flight conditions.

4.1.1. Longitudinal Autopilot

• Pitch Rate Damping

The natural damping of the short period mode predominantly arises from pitch rate induced angles of incidence. Thus, the damping is a function of the airspeed and the tailplane moment arm length. The aircrafts airspeed changes regularly during flight and the tailplane moment arm length is a function of the center of gravity location, which varies with fuel consumption. Artificial pitch rate damping is thus desired to desensitize the overall aircraft pitch rate damping to variations in these flight parameters, as well as to provide damping with respect to inertial space for wind gust disturbance rejection. Modal analysis was performed before and showed that the short period mode is orders of magnitude better controlled by the elevator than by the throttle. This suggests that simple feedback of the aircrafts pitch rate to the elevator will create an effective pitch rate damper. This feedback will essentially provide the aircraft with a larger tailplane during pitch rate perturbations. The control system is summarized in the block diagram of Figure 7.

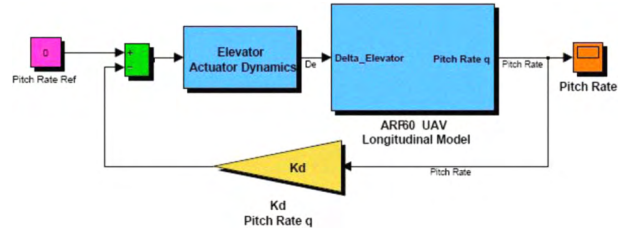


Figure 7: Pitch Rate Damping Block Diagram.

A feedback gain of $k_q = -0.11642$ increases the short period mode damping, which is deemed sufficient to adequately desensitize the pitch damping loop without exciting un-modelled dynamics.

• Pitch attitude hold using elevator

The aircrafts pitch attitude is regulated by the elevator actuator. Since the Phugoid oscillation cannot occur at constant pitch angle, a pitch-attitude-hold feature in the autopilot would be expected to suppress the Phugoid oscillations. The control system is shown in Figure 8 which includes an inner loop for SAS and an outer loop for the pitch attitude. PI controller was used in the outer loop to stabilize the UAV attitude. The PI gains parameters are found to be -1.1197 and -0.57 , respectively. The specifications for pitch step response are: rise time of under $2s$, overshoot of less than 8% and zero steady state error.

• Altitude hold using commanded pitch

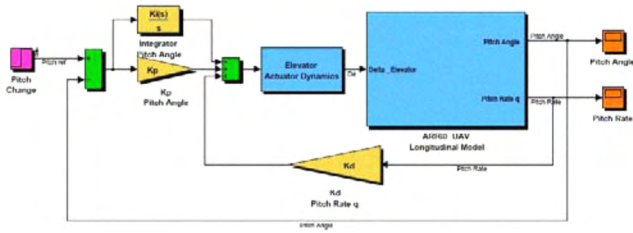


Figure 8: Pitch attitude hold using elevator Block Diagram.

The altitude controller is the only longitudinal trajectory controller. An outer loop which is the Altitude hold controller was added to the Pitch attitude hold using elevator to maintain level flight. Before the height error signal is fed to the Pitch attitude hold controller, it must be sent through a saturation block to ensure that it does not command climb rate signals in excess of $\pm 2m/s$. This block automatically ensures that the aircraft enters a constant climb rate mode when large altitude step commands are issued. The controller block diagram is shown in Figure 9 and their sets of gains are 0.4744 and 0.02224, respectively. The specifications for system step response are: rise time of less than 9 s, overshoot of less than 16% and zero steady state error.

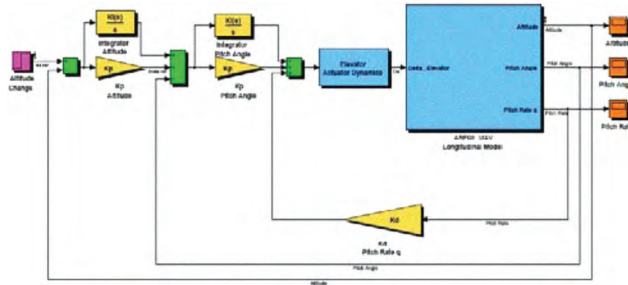


Figure 9: Altitude hold using commanded pitch Block Diagram.

• Airspeed hold using throttle

Figure 10 is the block diagram of the control loop for the forward airspeed (u) to maintain a constant speed along the flight path. The error between desired and actual speed is used to produce proportional displacement of the engine throttle so that the error is reduced. The PI gains parameters are found to be 0.02487 and 0.004564, respectively. The specifications for pitch step response are: rise time of fewer than 2s, overshoot of less than 1% and zero steady state error.

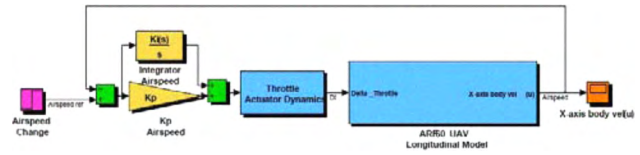


Figure 10: Airspeed hold using throttle Block Diagram.

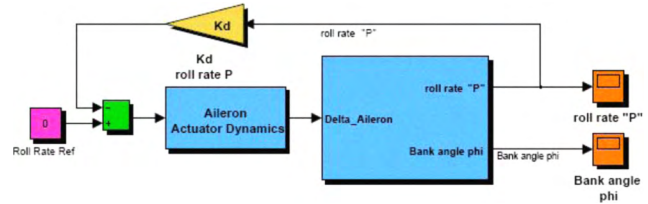


Figure 11: Roll Rate Damping Block Diagram

• Roll Attitude Hold

Feedback of the deviation of the roll angle to the ailerons (Figure 12) used to control the aircraft's roll angle thus the autopilot will hold the wings level.

• Dutch Roll Damper

Modal analysis has shown that the natural damping of the Dutch roll oscillation is low. Thus, a Dutch roll damper is implemented in order to suppress the natural oscillation. This will desensitize the overall yaw damping to variation in flight parameters and provide damping with respect to inertial space for wind gust disturbance. Modal analysis has shown that the rudder is 4 times more effective than the aileron in controlling the Dutch roll oscillation. Therefore the Dutch roll damping has been implemented by the controlling the rudder. The yaw rate signal must be high pass filtered before it is fed to the rudder, so that the damper does not counter the constant turn rate motions. A secondary advantage of the high pass filter is that it negates the bias effects of low cost rate gyroscopes. Figure 13 shows the Dutch roll damper block diagram.

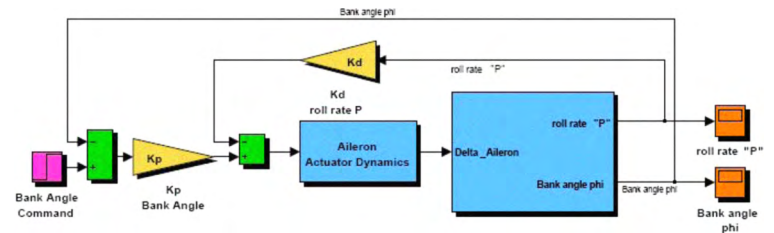


Figure 12: Roll Attitude Hold Block Diagram

4.1.2. Lateral Autopilot

• Roll Rate Damping

Closed loop control of roll rate (Figure 11) is used to reduce the variation of roll performance with flight conditions.

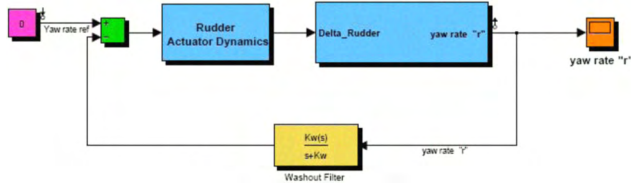


Figure 13: Dutch Roll Damper Block Diagram.

4.1.3. Trajectory Tracker(Shortest Flight Algorithm in 3D)

The bidirectional feedback guidance strategy (see Figure 14) was tuned, simulated and implemented. Details of this algorithm can be found in [3]. Figures 15, 16 and 17 shows the 2D, 3D plots and the states results of four waypoints (Hourglass) navigation using the extension of the Feedback Guidance Strategy - Bidirectional "simulation only" methods.

The results show that the aircraft reaches the desired waypoint dead on target. The reader must understand that these are simulated results, where all states are available for instantaneous feedback. Position, heading, altitude were available continuously with no sensor noise and no communication delays. Thus, the results achieved can be described as ideal. The Bang-Bang Trajectory Tracker with the SLC Autopilot completed the mission in less than 500 seconds. Overall the SLC Autopilot performed as expected and allowed a firm trajectory tracking.

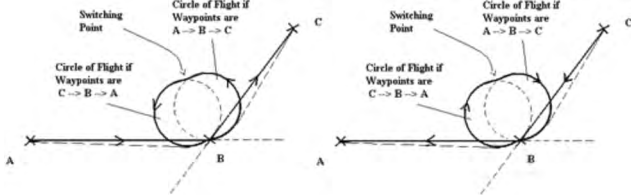


Figure 14: Extension of the Feedback Guidance Strategy - Bidirectional.

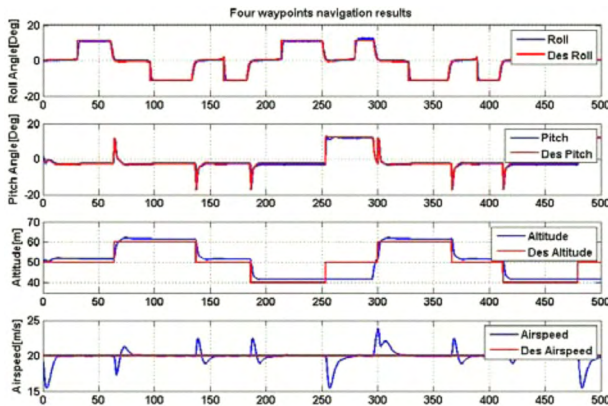


Figure 15: Four waypoints (hourglass) navigation results-States.

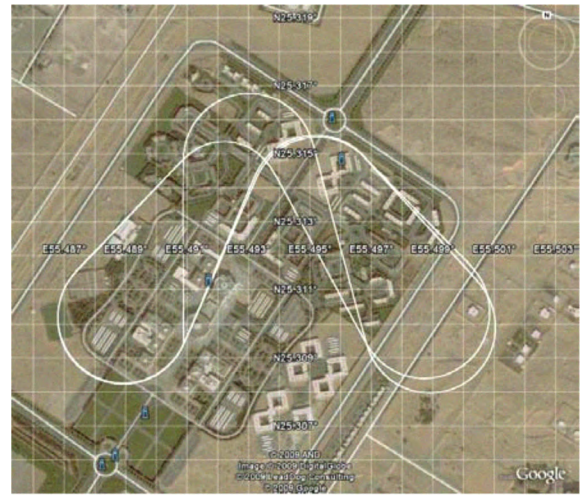


Figure 16: Four waypoints (Hourglass) navigation Map 2D.

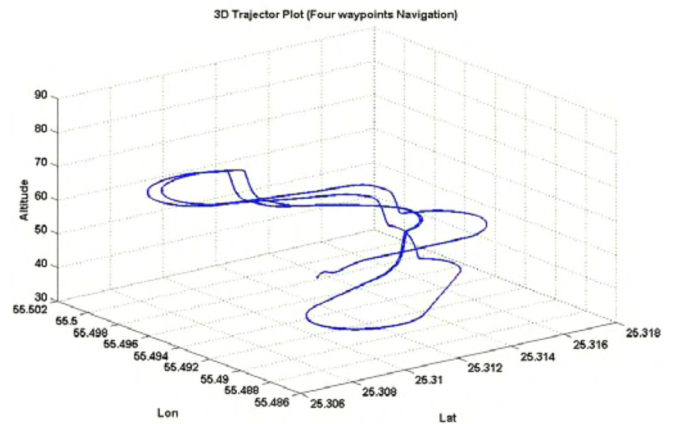


Figure 17: Four waypoints (Hourglass) navigation 3D Plot.

5. HARDWARE IN THE LOOP SIMULATIONS (HILS)

A hardware-in-the-loop simulation environment has been designed and built to validate hardware and software developments of the AUS ARF60 UAV autopilot. A full 6-DOF nonlinear dynamic model has been derived and key aircraft parameters have been measured or estimated. A batch parameter identification method has been implemented to determine the stability and control derivatives of the UAV using selected flight test data. Detailed models of the sensors and actuators were incorporated into the nonlinear simulation. Real-time 3-D simulator, with external pilot interface, has been designed to help with aircraft flight visualization. A block diagram illustrating the HILS main components is shown in Figure 18. Figure 19 shows the computers screens shots taken during the HILS simulation visualizing the dynamic behavior of the UAV, while displaying the corresponding state variables on the scopes.

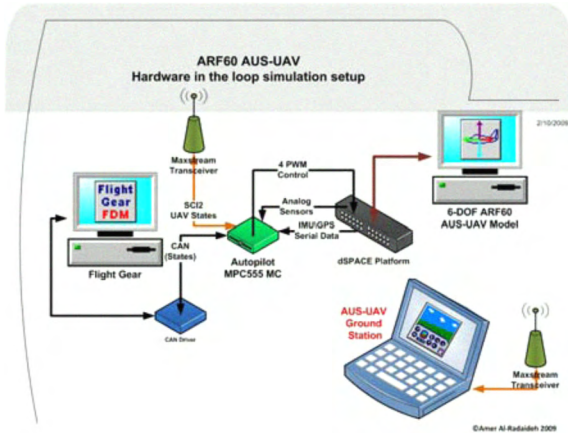


Figure 18: Hardware-in-the-loop (HIL) simulation Setup.

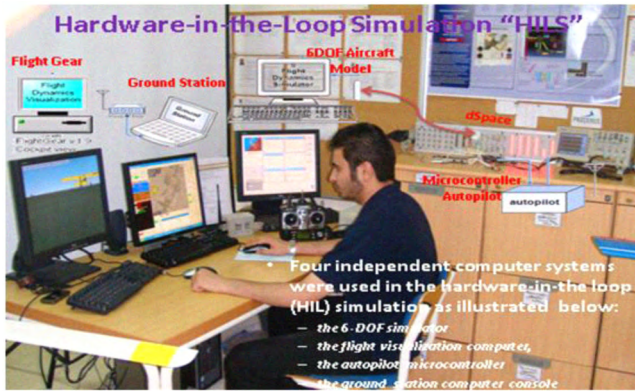


Figure 19: Hardware-in-the-loop (HIL) simulation environment

5.1. HILS Autopilot Results

Two tests were conducted to check the autopilot behavior. In those tests the wind disturbances were included; $[W_x = 5, W_y = -3, W_z = 0]$. The first test included; holding a fixed airspeed, fixed altitude and a bank angle commanded to a square wave with a specific amplitude and frequency. While, the second test included; holding fixed Airspeed, fixed bank angle and the altitude commanded to a sine wave with a specific amplitude and frequency.

5.1.1. HILS Autopilot Test 1

The first test holds the Airspeed to 20m/s, the altitude to 50m. The bank angle command shown in Figure 11 is a square wave with amplitude of 30° . The Bank angle was following the commanded one as Figure 20 shows the attitude results.

5.1.2. HILS Autopilot Test 2

The second test held the airspeed to 20m/s, bank angle to zero and the altitude commanded to a sine wave with 8m amplitude. Figure 21 shows that the actual altitude followed the sine command and the pitch angle was varying accordingly. The airspeed was held very close to the commanded value.

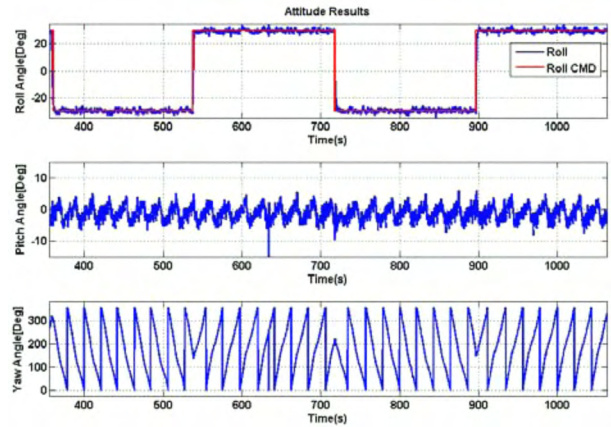


Figure 20: HILS Autopilot Test 1 -Attitudes.

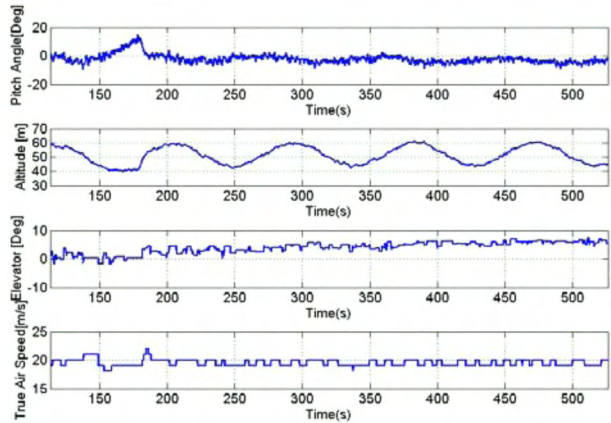


Figure 21: HILS Autopilot Test 2 - States Results.

5.2. HILS Trajectory Tracking Results

The Bidirectional Feedback Guidance Strategy Trajectory Tracker was tested using the HILS. Two navigation tests were conducted; the first one was two way point navigation while the second one is the hourglass shape (4 waypoints navigation). Figures 22, 23 show the 2D and 3D plots for the navigation between 2 waypoints with a distance of 500m in between. Furthermore, Figures 24, 25 show the 2D and 3D plots for the navigation between 4 waypoints in hourglass shape.

6. CONCLUSIONS

In this paper, the design, building, and testing of an integrated UAV test bed has been presented. The test bed includes an enhanced hardware in the loop simulation facility used to quickly model, design, and test the entire UAV avionics system. After integrating all avionics components on the bench, the user is capable of testing components, subsystems, or the whole system. Using this test bed, potential problems can be detected and fixed in the early stages of the design and therefore save time and effort.

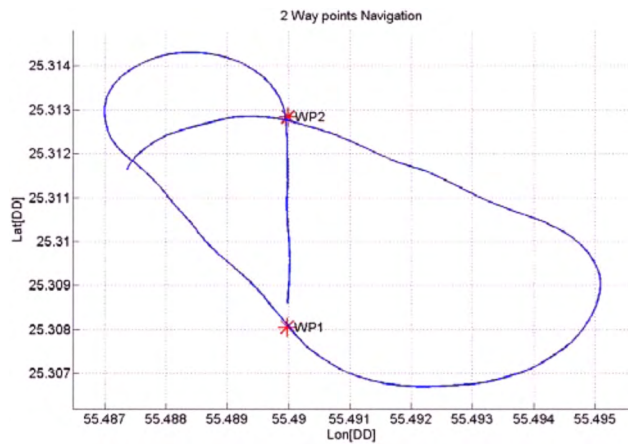


Figure 22: 2WP Navigation-2D.

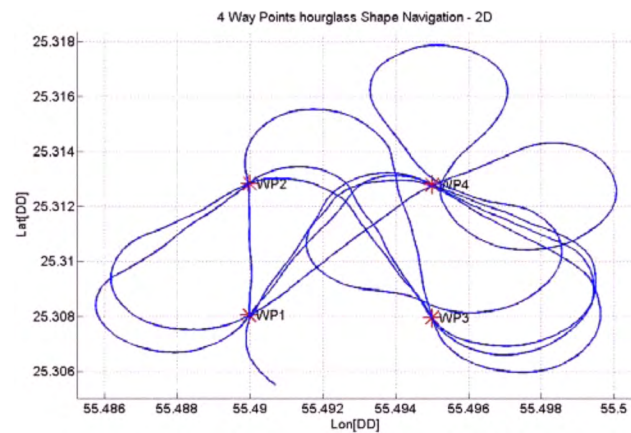


Figure 24: 4WP Navigation (Hourglass Shape) -2D.

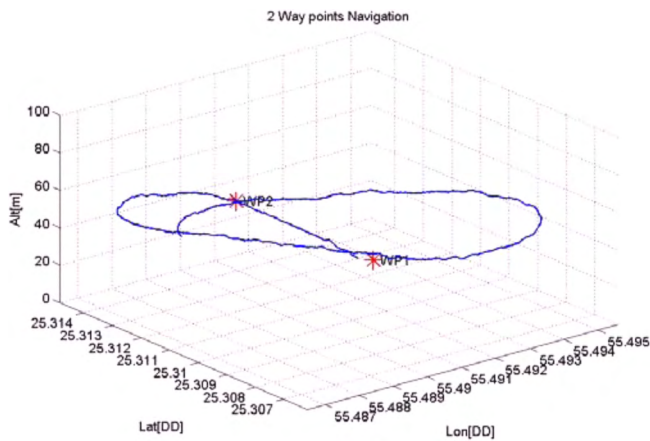


Figure 23: 2WP Navigation-3D.

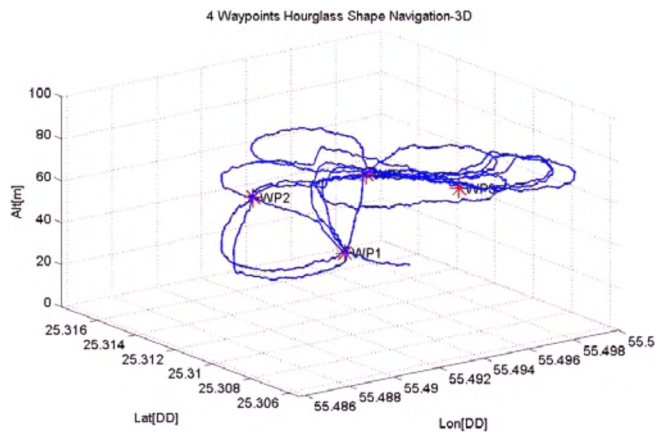


Figure 25: 4WP Navigation (Hourglass Shape)-3D.

A low cost avionics unit using commercial off the shelf components was designed, built, and tested. The designed avionics unit consisted of a variety of sensors made up of basic electronics components. The total cost of the developed unit was around 9,000 US dollars.

An augmented non-linear 6 DoF model of the aircraft has been developed. Stability and control derivatives were estimated based on the aircraft geometry. Both the engine and servo motors dynamics were estimated from test results using system identification techniques. Estimated subsystems were then integrated into the 6 DoF model and resulted in the augmented 6 Dof model.

A major effort went into the implementation of the Mathworks concept of rapid prototyping. The MPC5xx target from Freescale was used to embed code directly into the microprocessor from within the Simulink model. The Simulink Response Optimization, Control System Toolbox and Simulink Control Design were extensively used in the autopilot and guidance systems design.

A ground station, common to all AUS UAVs, was designed and built. The ground station has been developed using Visual Basic 2008. The designed interface consists of gauges to monitor

speed, altitude, and aircraft attitudes. It also includes a map that shows the position of the aircraft in the nearby area. Finally the GUI is used to upload commands directly to the aircraft.

Compared to the system previously used in the development of UAVs, a tangible savings in time and effort has been seen in using the new AUS UAV test bed.

7. REFERENCES

- [1] Brian L. Stevens, Frank L. Lewis "Aircraft Control and Simulation," JOHN WILEY & SONS, 2003.
- [2] Rauw, M. O. "Using SIMULINK for Nonlinear Analysis of Aircraft Control Systems," Delft University of Technology (Aerospace Engineering), 1992.
- [3] Al-Radaideh, Amer. "Guidance, Control and Trajectory Tracking of Small Fixed Wing Unmanned Aerial Vehicles (UAV's)," American University of Sharjah, Master's Thesis, 2009.
- [4] Robert, C. Nelson. "Flight Stability and Control, Aerospace and Mechanical Engineering Department, University of Notre Dame," McGRAW-HILL, 1990.
- [5] Vladislav. Klein, Eugene A. Morell "Aircraft System Identification: Theory and Practice," American Institute of Aeronautics and Astronautics, AIAA, 2006, 1st Edition.
- [6] Zadeh, L.A. "The Fuzzification of Systems," Springer Berlin / Heidelberg, Volume 216/2007, 2007.
- [7] Jung, S.J. "Autopilot Design for the Stanford DragonFly UAV: Validation through Hardware-in-the-Loop Simulation," AIAA, 2001.
- [8] LI-XIN WANG. "Design and analysis of fuzzy identifiers of nonlinear dynamic systems," IEEE transactions on automatic control, 1995.
- [9] Dongwon. Jung, Panagiotis. Tsiotras. "Modeling and Hardware-in-the-Loop Simulation for a Small Unmanned Aerial Vehicle," American Institute of Aeronautics and Astronautics, 2007.
- [10] Hadi, M. "Autopilot Design Based on Fuzzy Supervisory Controller for AUS-Autonomous Vehicle," American University Sharjah (AUS), Master's Thesis, 2005.
- [11] Hassan, M. "AUS-UAV Hils Setup of Dynamic Flight Path Planning," American University Sharjah (AUS), 2006.